AIMS *Mathematics*

AIMS Mathematics, 10(11): 27191–27216.
DOI: 10.3934/math.20251195
Received: 25 September 2025
Revised: 05 November 2025
Accepted: 12 November 2025
Published: 21 November 2025

https://www.aimspress.com/journal/Math

Research article

Fractional-order analysis of voltage and current propagation in lossy transmission lines with thermal feedback

Saqib Murtaza[1,2], Lilia El Amraoui[3], Aceng Sambas[1,2,4,*], Ahmed Mir[5], Chemseddine Maatki[6], Muhammad N. Khan[7,8,*], Badr M. Alshammari[9] and Lioua Kolsi[10]

[1] Faculty of Informatics and Computing, Universiti Sultan Zainal Abidin, Campus Besut, Terengganu, 22200, Malaysia
[2] Artificial Intelligence for Sustainability and Islamic Research Center (AIRIS), Universiti Sultan Zainal Abidin, Gongbadak, Terengganu, 21300, Malaysia
[3] Department of Electrical Engineering, College of Engineering, Princess Nourah bint Abdulrahman University, P.O. Box 84428, Riyadh 11671, Saudi Arabia
[4] Department of Mechanical Engineering, Universitas Muhammadiyah Tasikmalaya, Tamansari Gobras, Tasikmalaya, 46196, Indonesia
[5] Department of Chemical and Materials Engineering, College of Engineering, Northern Border University, Arar P.O. Box 1321, Saudi Arabia
[6] Department of Mechanical Engineering, College of Engineering, Imam Mohammad Ibn Saud Islamic University (IMSIU), Riyadh 11432, Saudi Arabia
[7] Jadara University Research Center, Jadara University, 21110, Jordan
[8] Institute of Engineering Mathematics, University Malaysia Perlis (UniMAP), 02600, Malaysia
[9] Department of Electrical Engineering, College of Engineering, University of Ha'il, Ha'il City 81451, Saudi Arabia
[10] Department of Mechanical Engineering, College of Engineering, University of Ha'il, Ha'il City 81451, Saudi Arabia

* **Correspondence:** Email: acengsambas@unisza.edu.my, nawazkhan@unimap.edu.my.

Abstract: Transmission lines form the backbone of power and communication networks, yet their behavior cannot be predicted by classical transmission line theory, which neglects thermal feedback and fractional-order dynamics. To address these limitations, we develop an advanced fractal-fractional electro-thermal model of a lossy transmission line to analyze voltage and current propagation under thermal feedback. The model is based on the fractal-fractional derivative in the sense of Caputo and

integrates the effects of series resistance, inductance, conductance, and capacitance together with temperature-dependent feedback. The coupled governing equations are derived as fractal-fractional order partial differential equations based on Kirchoff's current law (KCL) and Kirchoff's voltage law (KVL). The equations are solved numerically using the local radial basis functions (LRBF) scheme, a meshfree numerical technique, to investigate the spatio-temporal profiles of voltage, current, and temperature. The numerical results demonstrate that higher resistance and conductance increase both the attenuation and heating, while increasing capacitance reduces voltage propagation but enhances the current propagation. Furthermore, fractional and fractal orders enrich the analysis by introducing memory and dispersive effects. Overall, this study offers a more realistic and predictive framework for evaluating lossy transmission systems, with direct implications for improving reliability, thermal management, and performance in modern electrical and communication infrastructures.

Keywords: electro-thermal modeling; telegrapher's equations; fractional-order system; lossy transmission line; voltage and current propagation; thermal feedback
Mathematics Subject Classification: 34A08, 65M70, 94C05, 97Mxx

1. Introduction

Transmission lines are vital to both power and communication systems, serving as the primary conduit for electricity and data. In power networks, these lines carry electricity from power plants to homes, business, and industries, ensuring reliable and efficient delivery to consumers. Similarly, in communication systems, transmission lines serve as a medium of transmitting signals across networks, keeping communication tools such as phone, internet, and wireless systems running smoothly. The operational performance, stability, and reliability of these transmission lines rely solely on how transmission lines are designed and constructed. It is therefore important to accurately model the voltage and current propagation along the lossy transmission lines. In power networks, accurate modeling prevents energy loss, maintains the grid's stability, and address challenges such as faults, harmonic distortions, sudden demands fluctuations, and dynamics loads. Likewise, in communication systems, accurate modeling optimizes signal propagation, minimizes signal distortions and attenuation, and ensures high-quality data transmission [1–3]. In both systems, inaccurate and poor modeling may lead to inefficient system designs and systematic instabilities. Thus, advanced mathematical models and techniques are essential for ensuring the system' reliable and efficient performance. Talocia et al. [4] presented a transient analysis of lossy transmission lines with frequency dependent parameters. Their research work provides highly valuable results for the engineering sectors, as it offers a comprehensive benchmark dataset for analyzing lossy transmission lines. This benchmark also offers an efficient strategy for the evaluation of interconnected simulation tools. Gruodis et al. [5] examined the characterization and simulation of coupled lossy transmission line. Kannan et al. [6] proposed a model of transmission lines consisting of two-port coaxial terms for the characterization of dielectric materials. Their study highlights its strong potentials for industries and biomedical fields for transmitting signals with high precision. Additional studies highlighting the importance of analyzing lossy transmission lines can be found in [7–9].

In the 19th century, engineers came up with the idea of the classical telegrapher's equations, providing a foundational framework for analyzing the propagation of current and voltage in

transmission lines. These partial differential equations model the spatio-temporal distribution of voltage and current in transmission lines and integrates distributed parameters such as resistance, inductance, capacitance, and conductance. These equations enable the analysis of propagation delays, impedance matching, attenuation, and reflection phenomena in a wide range of applications [10]. Husain [11] investigated the electromagnetic conductivity of lossy transmission lines using a mathematical model of current and voltage propagation. Bamigbolo et al. [12] developed a mathematical model to analyze the propagation of electric current and the minimization of power losses in transmission lines. Their findings indicate that power losses will only be at a minimum when electricity is transmitted at a very low current and voltage. Korzyuk and Rudzko [13] proposed the first classical solution to the telegrapher's equations with non-linear potentials. Patil et al. [14] obtained a general solution of the telegrapher's equations using the Emad-Falih transformation. Hussein et al. [15] analyzed the telegrapher's equations through a numerical technique implemented in COMSOL Multiphysics. Alam et al. [16] examined the telegrapher's equations on metric graphs to address forward and control problems. Several other studies employing the classical mathematical model of the telegrapher's equations are documented in [17–20].

Despite their utility, these classical differential equations had some limitations and exhibited constraints. Their reliance on classical derivatives limits their abilities to capture subtle memory effects and the complex behavior of non-linear and high-frequency regimes. Additionally, they also ignore thermal coupling between electrical and thermal dynamics, which has substantial effects on the electrical performance of modern systems. Not considering these mechanisms restricts the classical model from achieving accurate predictions of attenuation and stability in practical scenarios. These limitations need advanced models, such as those that incorporate fractional calculus, and electro-thermal coupling to provide more accurate representation of the transmission lines' behavior under practical operating conditions. The fractional derivative operator has gained much attention over the last four decades due to its ability to capture heredity properties and complex anomalous diffusion in physical phenomena. However, its applications to the telegrapher's equations along with electro-thermal coupling in transmission lines remain largely unexplored. Even more rarely, researchers have sought to enrich this framework by considering fractal-fractional derivative operators, offering potential to capture memory, scaling, and non-local effects simultaneously. Most existing studies have employed a finite difference scheme or finite element analysis based on discretization to obtain numerical solutions. These approaches perform very well for local operators but encounter significant challenges when applied to fractional and non-local terms. To address these challenges meshfree methods, particularly the local radial basis functions (LRBF) scheme, offers greater adaptability in handling non-local terms within both regular and irregular geometries. However, their applications in the context of modeling electro–thermal transmission lines have received little attention to date. Therefore, to address this area of research, the authors have developed a mathematical model that integrates the electro-thermal effects with the fractal-fractional derivative in lossy transmission lines by using generalized telegrapher's equations. The time-based fractal-fractional derivative operator is considered in the Caputo sense, and the model is solved numerically using the LRBF scheme. The LRBF meshless formulation employs basis functions with compact support around each data point, which leads to well-conditioned and sparse system matrices. This localized structure significantly simplifies the selection of the shape parameter, thereby enhancing both numerical accuracy and computational efficiency in solving the resulting linear systems. In contrast to global (RBF) methods, which require dense matrices to be solved and are computationally demanding, the LRBF approach

generates sparse systems that can be efficiently handled using sparse linear algebra techniques. As a result, LRBF schemes offer superior stability, scalability, and accuracy, especially for large-scale or high-dimensional problems.

In this study, the multiquadric (MQ) RBF was selected due to its smoothness, flexibility, and proven capability in handling problems with complex fractional and fractal-fractional dynamics. The MQ function's tunable shape parameter allows a balanced trade-off between accuracy and conditioning; through numerical experimentation, an optimal parameter range was identified to ensure stable and highly accurate results across all tested configurations. Figure 1 illustrates the variation of the maximum real part of the eigenvalues with respect to the number of nodes, showing that the system remains stable as N increases. Similarly, Figure 2 presents the dependence of the eigenvalue spectrum on the shape parameter, confirming that stability improves and then saturates beyond a certain parameter range, indicating a robust choice of shape parameter for the MQ-LRBF formulation.

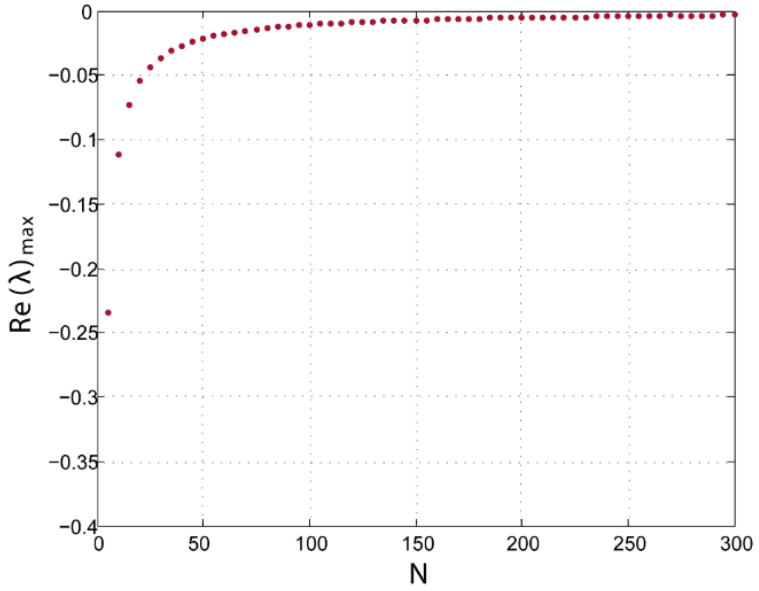

Figure 1. Plot of maximum real eigenvalues Re(λ) versus the number of nodes N.

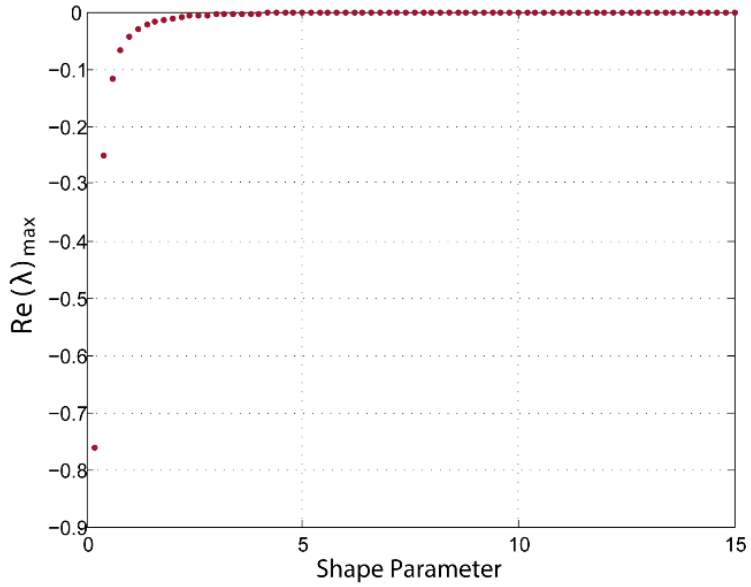

Figure 2. Plot of maximum real eigenvalues Re(λ) versus the shape parameter c.

2. Physical mathematical model

Assume a two-conductor line of length ℓ, modeled over an infinitesimal segment $[x,\ x+\Delta x]$ with the distributed parameters Resistance$R(T,w)\Delta x[\Omega]$, Inductance $L(T)\Delta x[H]$, shunt conductance $G(T,w)\Delta x[s]$, and capacitance $C(T,w)\Delta x[F]$. The local temperature $T=T(x,t)$ is assumed to be induced by self-heating and may vary with positions along the line. The terminal variables of voltage and current are defined by $v(x,t)$ and $i(x,t)$, respectively. The detailed overview is provided below in Figure 3.

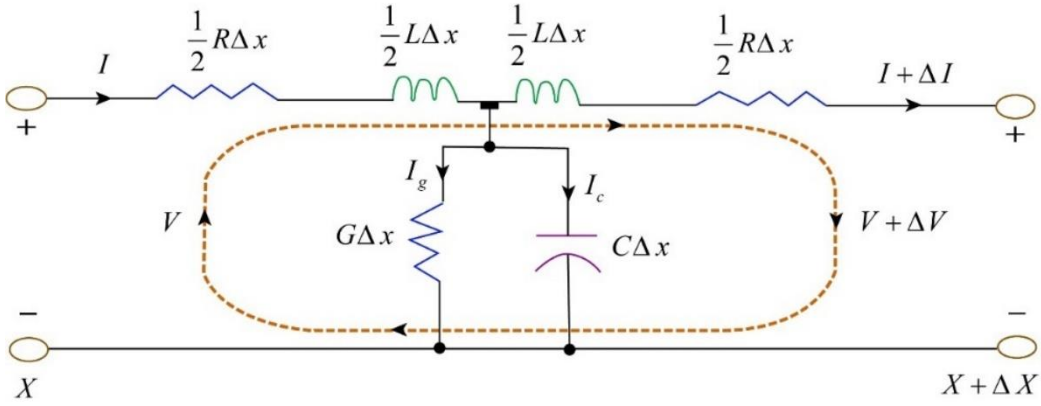

Figure 3. Graphical overview of the high-voltage transmission line based on an equivalent circuit.

By taking the limit $\Delta x \to 0$ and applying Kirchoff's voltage law (KVL) and Kirchoff's current law (KCL), the governing relations reduce to the classical telegrapher equations [21]:

$$\frac{\partial v(x,t)}{\partial x} = -L(T)\frac{\partial i(x,t)}{\partial t} - R(T,w)i(x,t), \tag{1}$$

$$\frac{\partial i(x,t)}{\partial x} = -C(T)\frac{\partial v(x,t)}{\partial t} - G(T,w)v(x,t). \tag{2}$$

The temporal and spatial evolution of the thermal field is described by the one-dimensional heat conduction equation which incorporates the effects of Joule and dielectric heating, and is expressed as:

$$\left(\rho C_p\right)\frac{\partial T(x,t)}{\partial t} = k\frac{\partial^2 T(x,t)}{\partial^2 x} + R(T,w)i^2(x,t) + G(T,w)v^2(x,t) - h(T(x,t) - T_\infty), \tag{3}$$

This heat equation connects electrical losses to thermal behavior and allows us to predict thermal performance and stability, as well as to locate where performance may deteriorate.

2.1. First-order fractal-fractional form

We introduced the fractal-fractional operator in the Caputo sense to extend the modelling framework. This operator provides an enhanced formulation that combines the principles of fractal geometry and fractional calculus and offers a powerful tool for capturing the memory effect, and non-local behavior in the governing equations. After incorporating the temporal fractal-fractional operator into Eqs (1–3), the governing equations takes the following forms:

$$\frac{\partial v(x,t)}{\partial x} = -L(T)\,{}^{FFC}D_t^{\alpha,\beta} i(x,t) - R(T,w)i(x,t), \tag{4}$$

$$\frac{\partial i(x,t)}{\partial x} = -C(T)\,{}^{FFC}D_t^{\alpha,\beta} v(x,t) - G(T,w)v(x,t), \tag{5}$$

$$\left(\rho C_p\right){}^{FFC}D_t^{\alpha,\beta} T(x,t) = k\frac{\partial^2 T(x,t)}{\partial^2 x} + R(T,w)i^2(x,t) + G(T,w)v^2(x,t) - \hat{h}(T(x,t) - T_\infty). \tag{6}$$

Here, ${}^{FFC}D_t^{\alpha,\beta} f(t)$represent fractal-fractional derivative operator in the Caputo sense [22].

$${}^{FFC}D_t^{\alpha,\beta} f(t) = \frac{1}{\Gamma(1-\alpha)}\frac{d}{dt^\beta}\int_0^t \frac{f(\tilde{\tau})}{(t-\tilde{\tau})^\alpha}\,d\tilde{\tau}\,, 0 < \alpha, \beta \leq 1,$$

where $0 < \alpha \leq 1$ denotes the fractional-order controlling the temporal memory effect; and $0 < \beta \leq 1$ represents the fractal dimension, which accounts for spatial heterogeneity and geometric irregularity within the physical domain and $\tilde{\tau}$denotes the integration variable.

Initial conditions

$$t = 0{:}\ v(x,0) = 0, i(x,0) = 0, T(x,0) = T_\infty, 0 \leq x \leq \ell. \tag{7}$$

Initially, the line is assumed to be unenergized, with both the voltage and current set to zero. This assumption is conventional in transient analysis and is compatible with the Caputo derivative framework, since only classical initial conditions are required. Furthermore, the line temperature is taken to be in thermal equilibrium with ambient surroundings.

Boundary conditions

At the source end:

$$(x = 0):\ v(0,t) = v_s(t),\ t > 0, \tag{8}$$

At the load end:

$$(x = \ell)\ v(\ell,t) = Z_L i(\ell,t),\ t > 0. \tag{9}$$

The input voltage to the line is set as $v_s(t)$, which make take the form of sinusoidal, pulse, or step input, among others. This specification enables the study of how a given voltage propagates through the fractal-fractional lossy line. The load terminal is connected to the impedance Z_L, which couples the voltage and current at the receiving end, thereby accounting for reflections that arise under a match $(Z_L = Z_0)$ or mismatch $(Z_L \neq Z_0)$.

Thermal boundary conditions

$$T(0,t) = T_\infty, T(\ell,t) = T_\infty, t > 0. \tag{10}$$

Here, T_∞ represents the ambient temperature.

The following dimensionless variables are introduced to simplify the governing equations and reduce the number of physical quantities involved in the analysis.

$$\hat{x} \to \frac{x}{l}, \hat{t} \to \frac{t}{\tau}, \hat{v} \to \frac{v}{V_0}, \hat{\imath} \to \frac{i}{I_0}, \hat{\Theta} = \frac{T-T_\infty}{\Delta T}, \tau = \sqrt{L_0 C_0}, I_0 = \frac{v_0}{Z_0}, Z_0 = \sqrt{\frac{L_0}{C_0}}. \tag{11}$$

By incorporating the dimensionless variables defined in Eq (11), the governing equations can be reformulated into their fractal-fractional dimensionless form, which is expressed as follows:

$$\hat{v}_x(\hat{x},\hat{t}) = -\hat{L}\big(\hat{\Theta}\big)^{FFC} D_t^{\alpha,\beta} \hat{\imath}(\hat{x},\hat{t}) - \hat{R}\big(\hat{\Theta}\big)\hat{\imath}(\hat{x},\hat{t}), \tag{12}$$

$$\hat{\imath}_x(\hat{x},\hat{t}) = -\hat{C}\big(\hat{\Theta}\big)^{FFC} D_t^{\alpha,\beta} \hat{v}(\hat{x},\hat{t}) - \hat{G}\big(\hat{\Theta}\big)\hat{v}(\hat{x},\hat{t}), \tag{13}$$

$$\hat{\Theta}_t(\hat{x},\hat{t}) = F_0 \hat{\Theta}_{xx}(\hat{x},\hat{t}) + J\frac{\hat{R}(\hat{\Theta})}{\hat{R}(0)}\hat{\imath}^2(\hat{x},\hat{t}) + \Lambda\frac{\hat{G}(\hat{\Theta})}{\hat{G}(0)}\hat{v}^2(\hat{x},\hat{t}) - B_i\hat{\Theta}(\hat{x},\hat{t}). \tag{14}$$

Correspondingly, the initial and boundary conditions can also be reformulated in a dimensionless framework. The resulting expressions are:

$$\hat{t} = 0:\ \hat{v}(\hat{x},0) = 0, \hat{\imath}(\hat{x},0) = 0, \hat{\Theta}(\hat{x},0) = 0. \tag{15}$$

At the source, they are

$$\hat{x} = 0,\ \hat{v}(0,\hat{t}) = v_s(\hat{t}), \hat{t} > 0, \tag{16}$$

At the end, they are

$$\hat{x} = 1,\ \hat{v}(1,\hat{t}) = \hat{Z}_L i_s(1,\hat{t}), \hat{t} > 0. \tag{17}$$

And the thermal boundary conditions are

$$\hat{\Theta}(0,\hat{t}) = 0, \hat{\Theta}(1,\hat{t}) = 0. \hat{t} > 0, \tag{18}$$

where $\hat{Z}_L = \frac{Z_L}{Z_0}$ is the load impedance normalized by the characteristic impedance Z_0.

During the dimensional analysis, the following physical dimensionless parameters are obtained:

$$\hat{R}(\hat{\theta}) = \frac{R(T,w)\ell}{Z_0}, \hat{L}(\hat{\theta}) = \frac{L(T)}{L_0}, \hat{G}(\hat{\theta}) = G(T,w)Z_0\ell, \hat{C}(\hat{\theta}) = \frac{C(T,w)}{C_0},$$
$$J = \frac{R_0 I_0^2 \tau}{\rho C_p \Delta T}, \Lambda = \frac{G_0 V_0^2 \tau}{\rho C_p \Delta T}, F_0 = \frac{k\tau}{\rho C_p \ell^2}, Bi = \frac{\tilde{h}\tau}{\rho C_p}.$$

Here, J, Λ, F_0, and Bi represent the Joule heating parameter, leakage heating parameter, Fourier number, and the Biot like number, respectively.

The model couples the electrical and thermal fields through Joule and dielectric heating effects. Temperature influences the electrical parameters (resistance, conductance), while these, in turn, affect the heat generation term. In order for the coupled system to remain mathematically stable and physically bounded, the following general conditions must be satisfied by the equations.

- The distributed parameters $\hat{R}, \hat{L}, \hat{G}, \text{and } \hat{C}$ and the thermal coefficients $J, F_0, Bi, \text{and } \Lambda$ are taken as positive definite, ensuring dissipative behavior of the system.
- The fractal-fractional orders $\alpha, \beta \in 0,1$ are chosen to preserve the boundedness of the operator ${}^{FFC}D_t^{\alpha,\beta}$, ensuring that energy dissipation dominates over amplification.
- The energy norm associated with the coupled system satisfies,

$$\frac{d\tilde{E}}{dt} \leq \delta\tilde{E} + Q(t),$$

where $\tilde{E}$ represents the total energy of the system, $\delta > 0$ is the damping rate, and $Q(t)$ is a bounded source term due to Joule and dielectric heating. In this case, the solution trajectories are bounded, and the system tends asymptotically to a steady state.

3. Numerical scheme

In this part of the manuscript, a thorough description of the numerical scheme and its application to the fractal-fractional model is provided.

3.1. Time discretization

The time derivative $\frac{\partial^\alpha \hat{v}(\hat{x},\hat{t})}{\partial \hat{t}^\alpha}$ is discretized using the Liouville-Caputo fractional derivative [23] for $\alpha \in (0,1)$, which is given by,

$$\frac{\partial^\alpha \hat{v}(\hat{x},\hat{t})}{\partial \hat{t}^\alpha} = \begin{cases} \frac{1}{\Gamma(1-\alpha)} \int_0^t \frac{\partial v(\hat{x},\tilde{\tau})}{\partial \tilde{\tau}} (\hat{t}-\tilde{\tau})^{-\alpha} d\tilde{\tau}, 0 < \alpha < 1, \\ \frac{\partial \hat{v}(\hat{x},\hat{t})}{\partial \hat{t}}, \alpha = 1. \end{cases} \tag{19}$$

Let $\hat{t}_0, \hat{t}_1, \ldots\ldots \hat{t}_H$ represent equally spaced time intervals within the range $[0,T]$, with $\hat{t}_h = h\eta$, where $h = 0,1,2,\ldots,H$. The time-step size is denoted by η. The fractional time derivative at the $(h+1)^{th}$ time level is approximated by,

$$\frac{\partial^{\alpha}\hat{v}(\hat{x},t_{h+1})}{\partial\hat{t}^{\alpha}}=\frac{1}{\Gamma(1-\alpha)}\int_{0}^{t_{h+1}}\frac{\partial\hat{v}(\hat{x},\tilde{\tau})}{\partial\tilde{\tau}}(\hat{t}_{h+1}-\tilde{\tau})^{-\alpha}d\tilde{\tau},$$

$$\approx\frac{1}{\Gamma(1-\alpha)}\sum_{s=0}^{h}\int_{s\eta}^{(s+1)\eta}\frac{\partial\hat{v}(\hat{x},\tilde{\tau}_{s})}{\partial\tilde{\tau}}(\hat{t}_{s+1}-\tilde{\tau})^{-\alpha}d\tilde{\tau}, \tag{20}$$

By performing the integration, we get the approximation

$$\frac{\partial^{\alpha}\hat{v}(\hat{x},\hat{t}_{h+1})}{\partial\hat{t}^{\alpha}}\approx\begin{cases}a_{0}\left(\hat{v}^{h+1}-\hat{v}^{h}\right)+a_{0}\sum_{s=1}^{h}b\ \ \left(\hat{v}^{h+1-s}-\hat{v}^{h-s}\right),h\geq 1,\\ a_{0}(\hat{v}^{1}-\hat{v}^{0}),h=0,\end{cases} \tag{21}$$

where $a_0=\frac{\eta^{-\alpha}}{\Gamma(2-\alpha)}$ and $b_s=(s+1)^{1-\alpha}-s^{1-\alpha}$, for $s=0,1,2,\ldots\ldots,h$.

3.1.1. Implementation of the LRBF scheme

In this study, we utilize the LRBF scheme [24] to solve the governing equations of the system. This method is particularly effective for solving complex, non-linear partial differential equations (PDEs) in a mesh-free manner. For each node $\hat{x}_j$ a local support region is defined by selecting a set of n_j neighboring points from the set of all points $\{\hat{x}_1,\hat{x}_2,\ldots\ldots\hat{x}_{N^n}\}$, with $n_j\ll N^n$, ensuring that the support domain around each node is compact. The m^{th}-order derivative at node $\hat{x}_j$ is approximated as a weighted sum of the values at the neighboring points:

$$\hat{v}^{(m)}\left(\hat{x}_j\right)\approx\sum_{k=1}^{n_j}\lambda_k^{(m)}\hat{v}\left(\hat{x}_{jk}\right), \tag{22}$$

where the $\lambda_k^{(m)}$ are the unknown weighting coefficients to be determined.

The coefficients $\lambda_k^{(m)}$ are calculated by solving a system that involves the LRBF $\psi^{(m)}\left(\left\|\hat{x}_j-\hat{x}_l\right\|\right)$, which are used to express the approximation for the m^{th} derivative at the neighboring nodes. The relation is given by,

$$\psi^{(m)}\left(\left\|\hat{x}_j-\hat{x}_l\right\|\right)=\sum_{k=1}^{n_j}\lambda_{jk}^{(m)}\psi\left(\left\|\hat{x}_{jk}-\hat{x}_l\right\|\right),l=j_1,j_2,\ldots\ldots j_{n_j}. \tag{23}$$

In matrix form, the equation above is represented as follow:

$$\Psi^{(m)}=A\lambda^{(m)}, \tag{24}$$

where $\Psi^{(m)}=\left[\psi_{j_1}^{(m)}\left(\hat{x}_j\right),\ldots\ldots,\psi_{j_{nj}}^{(m)}\left(\hat{x}_j\right)\right]^T$ represents the RBF values at the neighboring nodes, $\lambda^{(m)}=\left[\lambda_{j_1}^{(m)},\ldots\ldots\ldots,\lambda_{j_{nj}}^{(m)}\right]^T$ is the vector of unknown coefficients, and the matrix A is defined as $A_{kl}=\psi\left(\left\|\hat{x}_{jk}-\hat{x}_{jl}\right\|\right)$, which maintains the RBF distances between each pair of neighboring nodes.

The system of equations for the coefficients $\lambda_k^{(m)}$ is solved by:

$$\lambda^{(m)} = A^{-1}\Psi^{(m)}. \tag{25}$$

Finally, the derivative approximation at the node y_j is obtained by taking the weighted sum of the values of the function $\hat{v}(\hat{x}_k)$ at the neighboring nodes, yielding:

$$\hat{v}^{(m)}(\hat{x}_j) = \left(\lambda^{(m)}\right)^T V_{nj}, \tag{26}$$

where $V_{nj} = \left[\hat{v}(\hat{x}_{j_1}), \ldots\ldots, \hat{v}\left(\hat{x}_{j_{nj}}\right)\right]^T$ is the vector of function values at the neighboring nodes. This local RBF method offers a robust and flexible approach for solving differential equations in a mesh-free environment, making it highly suitable for complex geometries and problems involving irregular domains.

3.1.2. The weighted scheme

In this section, the $\boldsymbol{\theta}$-weighted scheme is applied to the governing equation, and the time-fractional derivative is substituted using the discretization method. This results in the following equation:

$$a_0\hat{v}^{\hbar+1} - \theta\pounds\hat{v}^{\hbar+!} = \begin{cases} a_0\hat{v}^{\hbar} + (1-\theta) - a_0\sum_{s=1}^{\hbar} b_s\left(\hat{v}^{\hbar-s+1} - \hat{v}^{\hbar-s}\right), \hbar \geq 1; \\ a_0\hat{v}^{0} + (1-\theta)\pounds(\hat{v}^{0}), \hbar = 0. \end{cases} \tag{27}$$

Next, the meshless method is employed, where the value of $\hat{v}\left(\hat{x}, \hat{t}^{\hbar+1}\right)$ is interpolated using the LRBF scheme. Substituting the values obtained from the LRBF scheme leads to the following expression:

$$(a_0 I - \theta\pounds)\hat{v}^{\hbar+1} = \begin{cases} (a_0 I + (1-\theta)\pounds)\hat{v}^{\hbar} - a_0\sum_{s=1}^{\hbar} b_s\left(\hat{v}^{\hbar-s+1} - \hat{v}^{\hbar-s}\right), \hbar \geq 1; \\ (a_0 I + (1-\theta)\pounds)\hat{v}^{0}, \hbar = 0. \end{cases} \tag{28}$$

Rearranging the terms and simplifying the notation, we obtain the final form.

$$(a_0 I - \theta L)\hat{v}^{\hbar+1} = \begin{cases} (a_0 I + (1-\theta)\pounds)\hat{v}^{\hbar} - a_0\sum_{s=1}^{\hbar} b_s\left(\hat{v}^{\hbar-s+1} - \hat{v}^{\hbar-s}\right), \hbar \geq 1; \\ (a_0 I + (1-\theta)L)\hat{v}^{0}, \hbar = 0, \end{cases} \tag{29}$$

where I represents the identity matrix, and L denotes the weight matrix associated with the differential operator $\pounds$.

Finally, the solution at the next time level $\hat{t}^{\hbar+1}$ is computed using the following expression:

$$V^{\hbar+1} = M^{-1}NV^{\hbar} + M^{-1}G^{\hbar+1}, for \hbar \geq 0, \tag{30}$$

where the matrices are defined as:

$$M = a_0 I - \theta L, N = a_0 I + (1-\theta)L, \tag{31}$$

The vector $G^{\hbar+1}$ is given by,

$$G^{\hbar+1} = G_1^{\hbar+1} + G_2^{\hbar+1}, for \hbar \geq 0. \tag{32}$$

The components of $G^{\hbar+1}$ are

$$G_1^{\hbar+1} = \left(g_1^{\hbar+1}, 0, \ldots, g_2^{\hbar+1}\right) \text{ and } G_2^{\hbar+1} = -a_0 \sum_{s=1}^{\hbar} b_s \left(V^{\hbar-s+1} - V^{\hbar-s}\right), \tag{33}$$

where $g_1^{\hbar+1}$ and $g_2^{\hbar+1}$ are the known functions determined by the boundary conditions (BCs). The scheme in Eq (30) is then used to compute the solution at any desired time level $\hat{t}^{\hbar}$.

3.1.3. Stability and convergence

The scheme presented in Eq (30) is essentially a recurrence relation that computes the solution at the time η^{s+1} based on the solution at the time η^s. The matrix $E = M^{-1}N$ is referred to as the amplification matrix, and its elements depend on the constant $\kappa = \frac{d\eta}{h^{\zeta}}$, where $d\eta$is the time step, h is the spatial distance between two consecutive nodes, and ζ is the order of the spatial differential operator. Let u^s represent the exact solution of the model equation at time η^s.

Theorem 1. Let $\Omega \subseteq \Re^r$ be a bounded, open set that satisfies an interior cone condition. Assume that $\Phi \in C^{2\kappa}(\Omega \times \Omega)$ is symmetric and strictly conditionally positive definite of order $m$on $\Re^r$. The interpolant to a function $f \in N_{\phi}(\Omega)$, based on the $(m-1)$-unisolvent set χ, is denoted by P_f. If we fix $\gamma \in \mathbb{N}_0^r$ with $|\gamma| \leq \kappa$, then there exist positive constants C and h_0 (independent of x, f, and, Φ) exist such that the following inequality holds:

$$\left|D^{\gamma} f(x) - D^{\gamma} P_f(x)\right| \leq C h_{\chi,\Omega}^{\kappa-|\gamma|} \sqrt{C_{\Phi}(x)} \left|f N_{\phi}(\Omega)\right|, \tag{34}$$

provided that $h_{\chi,\Omega} \leq h_0$. The term $C_{\Phi}(x)$ is defined as:

$$C_{\Phi}(x) = \max_{\substack{\gamma,\alpha \in N_0^r \\ |\gamma|+|\alpha|=2\kappa}} \max_{w,y \in \Omega \cap B(x, c_2 h\chi, \Omega)} \left|D_1^{\gamma} D_1^{\alpha} \Phi(w, y)\right|. \tag{35}$$

For complete proof, refer to [25].

By applying Theorem 1 to infinitely smooth functions such as the GA (generalized approximation) or the generalized (inverse) MQ (multiquadric) RBFs, we immediately obtain arbitrarily high algebraic convergence rates. Specifically, for every $\kappa \in \mathbb{N}$ and $|\gamma| \leq \kappa$, the following inequality holds:

$$\left|D^{\gamma} f(x) - D^{\gamma} P_f(x)\right| \leq C h^{\kappa-|\gamma|} \left|u N_{\phi}(\Omega)\right|, \tag{36}$$

where $f \in N_{\phi}(\Omega)$ represents the native space of RBFs. Extensive studies have been conducted to explore the dependence of the constant C_{κ} on κ [26].

In this study, the MQ RBF is utilized, leading to the conclusion that:

$$|D^{\gamma}U(x) - D^{\gamma}u(x)| \leq C_{\kappa}h^{\kappa-|\gamma|}\left|UN_{\phi}(\Omega)\right|. \tag{37}$$

Next, suppose that the scheme (30) is p^{th}-order accurate in space. We then have the following approximation:

$$u^{s+1} = Eu^{s} + AM^{-1}G^{s+1} + o((d\eta)^{2-\gamma} + h^{p}), d\eta, h \to 0. \tag{38}$$

Let $\in^{s} = u^{s} - U^{s}$ represent the residual. Then the residual at the next time step is given by:

$$\in^{s+1} = E \in^{s} + o((d\eta)^{2-\gamma} + h^{p}), d\eta, h \to 0. \tag{39}$$

According to Lax-Richtmyer's stability conditions [27], the scheme (30) is stable if

$$\|E\| \leq 1, \tag{40}$$

where E is a normal matrix; and in this case, $\|E\| = \gamma(E)$. Otherwise, the inequality $\gamma(E) \leq \|E\|$ always holds. Assuming that the step size h is sufficiently small, and that the solution and initial conditions of the problem are sufficiently smooth, we must ensure that $d\eta \to 0$ in such a way that the ratio $\kappa = \frac{d\eta}{h^{p}}$ remains constant. Thus, there exists a constant C such that:

$$\|\in^{s+1}\| \leq \|E\|\|\in^{s}\| + C((d\tau)^{2-\gamma} + h^{p}), s = 0,1,2,\ldots,T \times M. \tag{41}$$

Since the residual $\in^{s}$ satisfies the zero initial conditions and the boundary conditions, $\in^{0} = 0$, we can use mathematical induction to show that

$$\|\in^{s+1}\| \leq (1 + \|E\| + \|E\|^{2} + \ldots + \|E\|^{s-1})C((d\tau)^{2-\gamma} + h^{p}), s = 0,1,2,\ldots.T \times M. \tag{42}$$

Using the conditions from Eq (40), we conclude that

$$\|\in^{s+1}\| \leq sC((d\tau)^{2-\gamma} + h^{p}), s = 0,1,2,\ldots.,T \times M. \tag{43}$$

Thus, the scheme is convergent.

4. Results and discussion

In this section, the numerical results obtained from the electro-thermal fractal-fractional transmission line model are presented. The results emphasize the sensitivity of voltage and current propagation in a lossy transmission line with thermal feedback under the influence of key physical parameters. Particular attention is devoted to the distributed parameters $\hat{R}$ $\hat{L}$ $\hat{G}$ and $\hat{C}$, which directly govern both the electrical propagation and thermal distribution within the line. The numerical simulations are performed using the LRBF scheme, which offers a stable and efficient computational framework for investigating how these parameters influence the amplitude and phase of voltage within the transmission line. The key results, together with their physical and scientific interpretation, are discussed below.

Figures 4 and 5 are plotted to examine the influence of increasing values of series resistance $\hat{R}$ on voltage and current propagation in transmission lines. Both figures show a decline in voltage and current propagation in the transmission line. Series resistance $\hat{R}$ indicates the Ohmic loss per unit of length. When the value of the parameter $\hat{R}$ increases, part of the electromagnetic wave's energy is converted into heat, so less electromagnetic energy remains to maintain the voltage and current

amplitude downstream. Moreover, increasing values of $\hat{R}$ significantly increase the attenuation, which accelerates the exponential decay in voltage and current propagation. Therefore, declines in propagations are observed for higher values of $\hat{R}$.

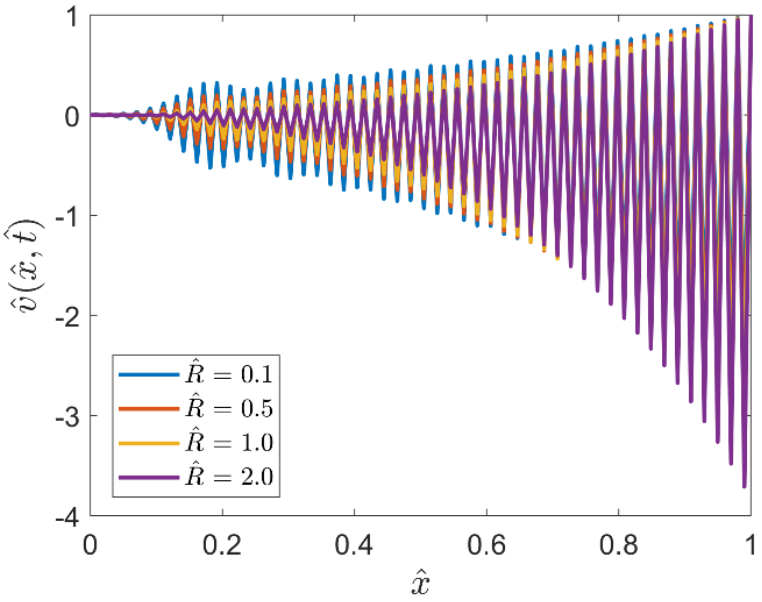

Figure 4. Voltage propagation versus series resistance $\hat{R}$, when $\alpha = 0.5, \beta = 0.5, \hat{L} = 0.75, \hat{G} = 0.15,$ and $\hat{C} = 0.75$.

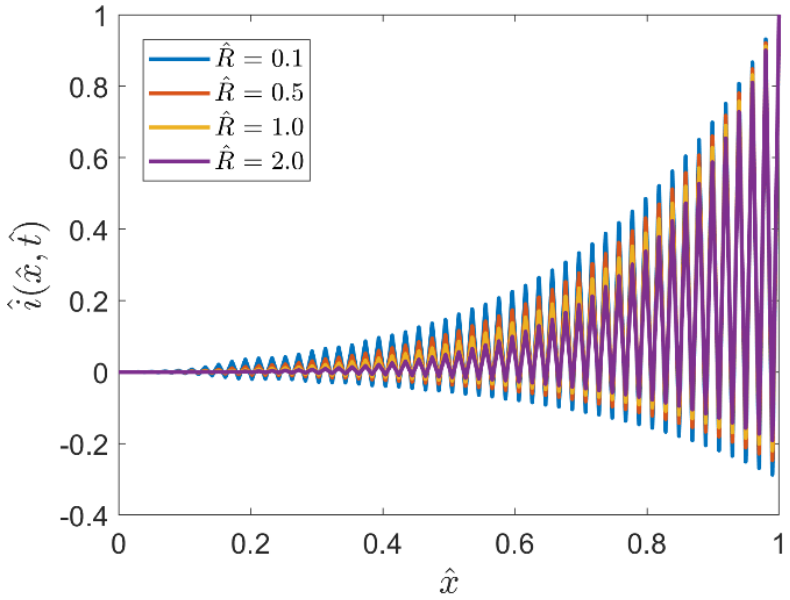

Figure 5. Current propagation versus series resistance $\hat{R}$ when $\alpha = 0.5, \beta = 0.5, \hat{L} = 0.75, \hat{G} = 0.15,$ and $\hat{C} = 0.75$.

Figures 6 and 7 have been plotted to examine the influence of increasing the magnitude of inductance $\hat{L}$ on voltage and current propagations in a fractal-fractional lossy transmission line. Both figures reveal that an increasing inductance leads to a decline in voltage and current propagation in a lossy transmission line. An increasing magnitude of $\hat{L}$ indicates that line has stronger magnetic energy storage, which provides resistance to the waves' propagations and alters the balance of impedance. As a result, the waves struggle to sustain convert voltage and current variations as propagation signals, and thus we observe a delayed voltage and current profile.

Figures 8 and 9 demonstrate the impact of the increasing magnitude of shunt conductance $\hat{G}$ on voltage and current propagation in a fractal-fractional lossy transmission line. The figures clearly show that both voltage and current propagation in a transmission line decline for higher values of $\hat{G}$. Higher values of $\hat{G}$ imply that more current is diverted from the traveling waves, leading to a reduction in the longitudinal electromagnetic energy, and thus reducing voltage and current propagation. From a mathematical perspective, the shunt conductance $\hat{G}$ is directly proportional to the attenuation constant, so greater values of $\hat{G}$ produce a more rapid exponential decay in the amplitude of voltage along the line, and hence we observe decreasing profiles of voltage and current propagation in the transmission line. For engineers, understanding the sensitivity to $\hat{G}$ guides material and geometry choices, cooling and protection design, condition monitoring strategies, and maintenance planning to preserve the integrity of voltage and service life.

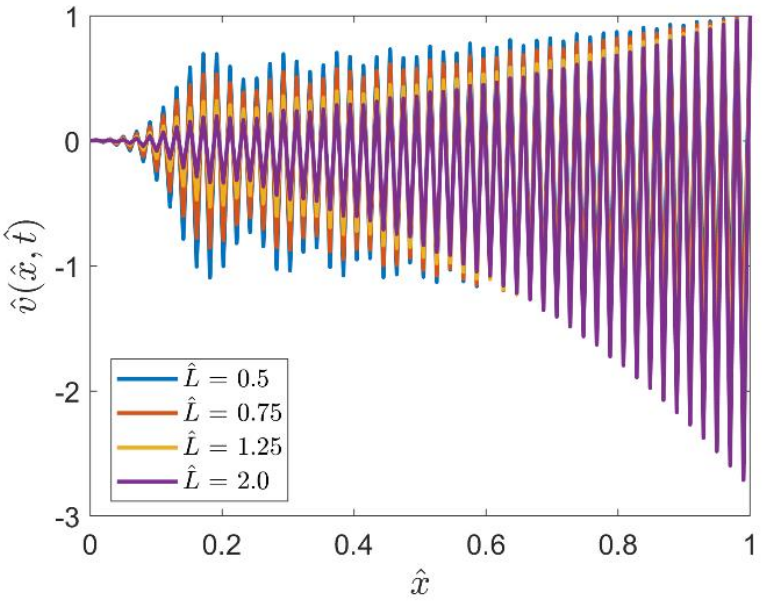

Figure 6. Voltage propagation versus series resistance $\hat{L}$ when $\alpha = 0.5, \beta = 0.5, \hat{R} = 0.5, \hat{G} = 0.15,$ and $\hat{C} = 0.75$.

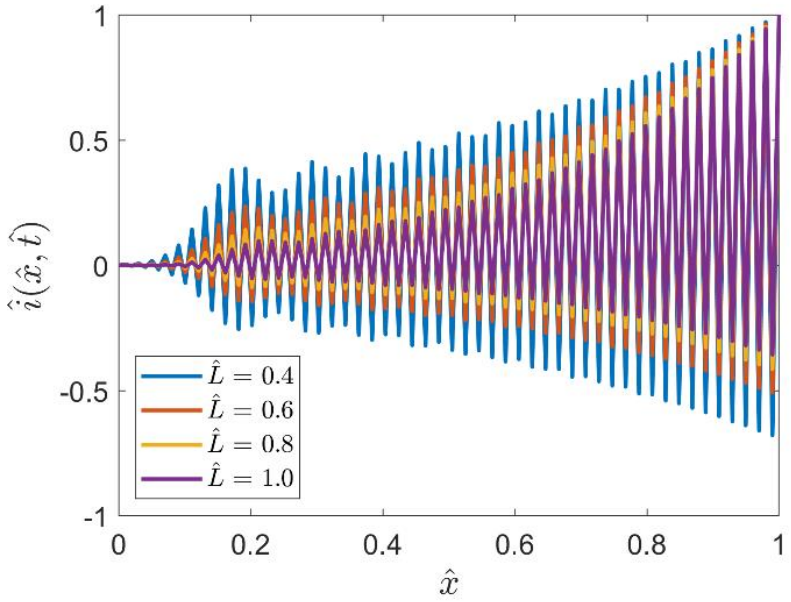

Figure 7. Current propagation versus series resistance $\hat{L}$ when $\alpha = 0.5, \beta = 0.5, \hat{R} = 0.5, \hat{G} = 0.15,$ and $\hat{C} = 0.75$.

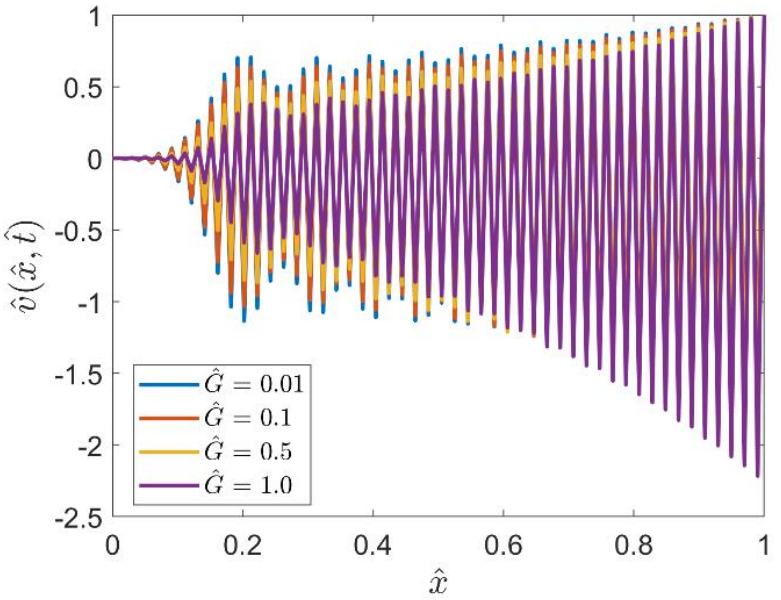

Figure 8. Voltage propagation versus series resistance $\hat{G}$, when $\alpha = 0.5, \beta = 0.5, \hat{R} = 0.5, \hat{L} = 0.75,$ and $\hat{C} = 0.75$.

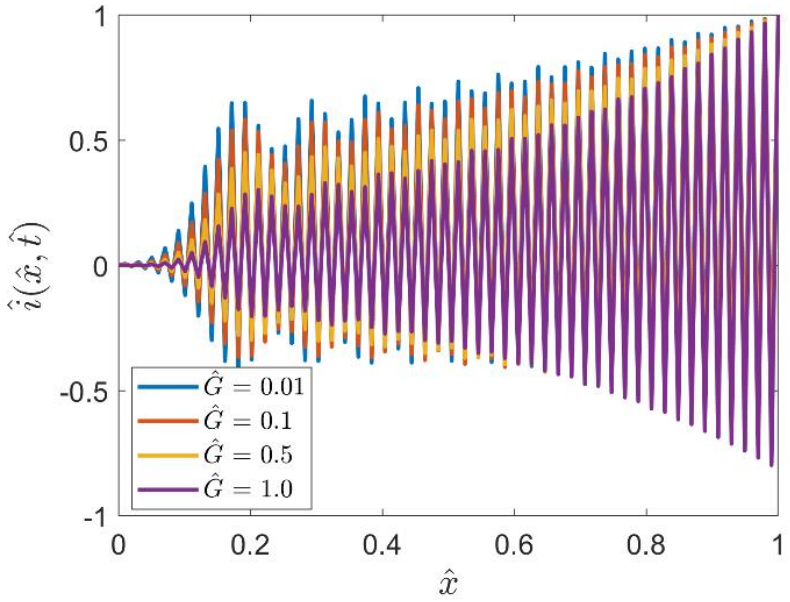

Figure 9. Current propagation versus series resistance $\hat{G}$, when $\alpha = 0.5, \beta = 0.5, \hat{R} = 0.5, \hat{L} = 0.75,$ and $\hat{C} = 0.75$.

The influence of capacitance $\hat{C}$ on voltage and current propagation in lossy transmission lines has been plotted in Figures 10 and 11. Both figures clearly indicate declining profiles for higher magnitudes of $\hat{C}$. However, in the case of current propagation, the profile initially shows an increasing pattern, but with the passage of time, it tends towards a decreasing profile; so in conclusion, the current propagation profile is also a decreasing function of larger values of $\hat{C}$. This behavior in both the profile is physically consistent, as increasing values of capacitance directly affect the impedance, which causes slow wave propagation and thereby, we observe a delayed propagation profile for both the voltage and current.

Figure 12 illustrates a comparison between the present (classical) solution and the solution reported by Abro et al. [21]. Both the normalized current profiles $\hat{\imath}(\hat{x},\hat{t})$, plotted along the $\hat{x}$-axis, show the excellent overlap of two solutions. The closed correspondence of the oscillatory patterns verifies that the present model maintains consistency with theoretical predictions. It also further validates the accuracy of the present numerical scheme.

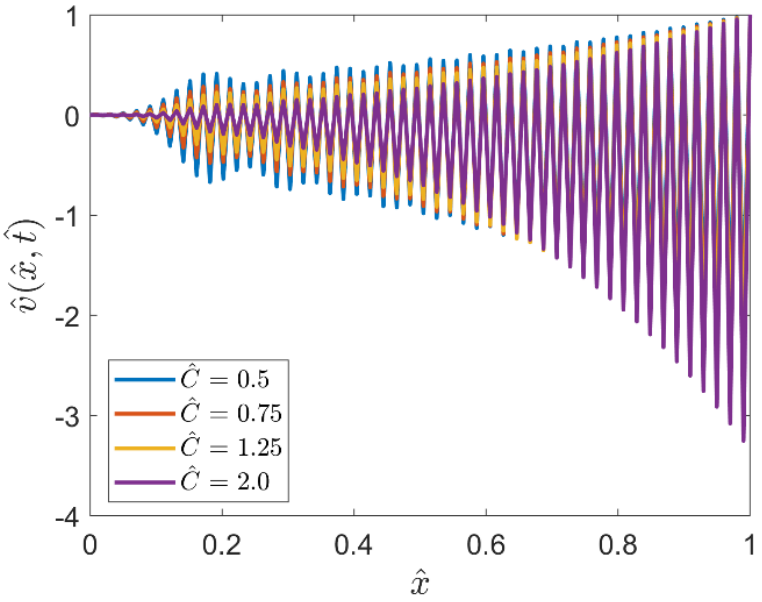

Figure 10. Voltage propagation versus series resistance $\hat{C}$ when $\alpha = 0.5, \beta = 0.5, \hat{R} = 0.5, \hat{L} = 0.75,$ and $\hat{G} = 0.15$.

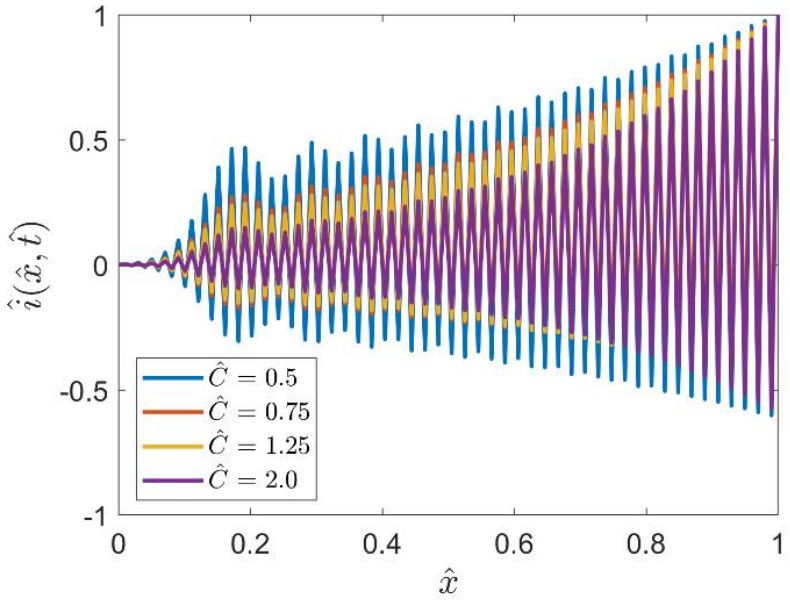

Figure 11. Current propagation versus series resistance $\hat{C}$ when $\alpha = 0.5, \beta = 0.5, \hat{R} = 0.5, \hat{L} = 0.75,$ and $\hat{G} = 0.15$.

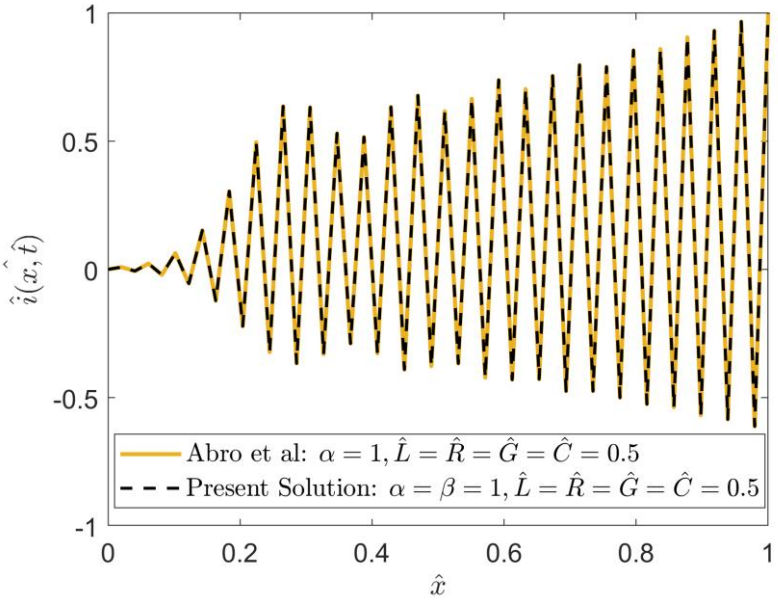

Figure 12. Comparative analysis between the present (classical) solution and that of Abro et al. [21].

Figure 13 demonstrates how the fractional-order parameter α contributes to the thermal analysis of lossy transmission lines. The figure provides multiple integral curves for different values of the fractional order α and shows that the thermal profile is an increasing function of the fractional order. The fractional order derivative introduces memory effects, meaning that the rate of temperature change depends not only on the present gradient but also on the whole history of the system. The incorporation of fractional derivatives provides an advanced mathematical framework for modeling and examining thermal behavior in lossy transmission lines. Unlike conventional integer-order models that rely upon purely local and memoryless conduction, fractional derivatives incorporate the dependence on the underlying history, non-local behavior, and anomalous diffusion. Therefore, temperature increases, cooling, and temperature distribution can be better modeled under realistic operating conditions. From an engineering point of view, fractional models would improve prediction of thermal estimation, reliability checking, and safety factors, therefore contributing to the good design, operation and optimization of power transmission systems. However, transmission lines' surfaces are not smooth cylindrical shapes, as the strand layout and surface degradation give them a fractal like surface, which make them complex from geometrical perspective. Therefore, the inclusion of fractal order derivative in the model offers a framework to study the fractal-like surface of the transmission lines more effectively. Increasing the fractal order significantly enhances the convective heat transfer coefficient, leading to improved cooling efficiency under certain conditions. Classical thermal models are based on the assumption of smooth surfaces and a homogeneous heat transfer, which may lead to incorrect temperature estimation. By including a fractal order that considers surface roughness, geometric complexity, and memory effects in terms of fractional derivatives, the models provide a more realistic representation of actual conductors, ensuring more accurate steady-state and transient thermal profiles.

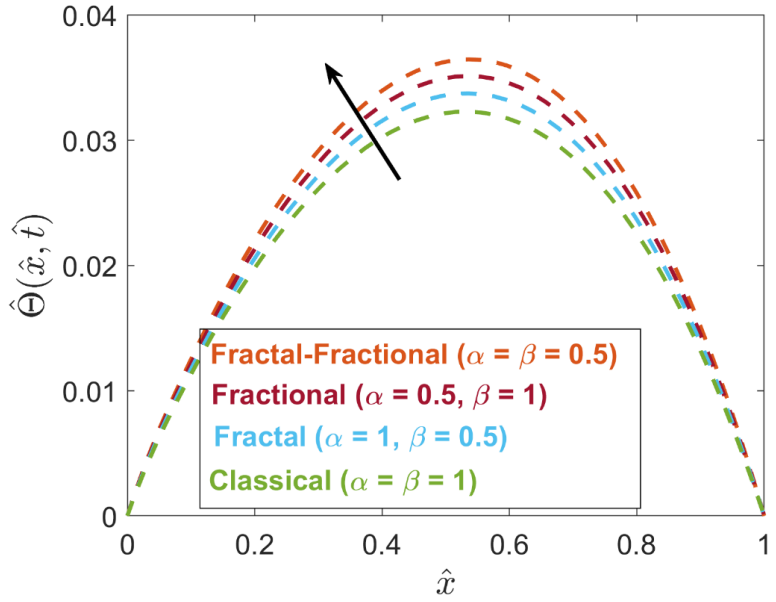

Figure 13. Comparative analysis of classical, fractional, and fractal-fractional order thermal field when $F_0 = 0.4, J = 0.5, \Lambda = 0.6,$ and $Bi = 02$.

Figure 14 illustrates the influence of the thermal Fourier number F_0 on thermal distribution. The figure shows an increasing trend in the thermal profile with higher values of F_0. The thermal Fourier number is a dimensionless parameter and represents the ratio of heat conduction to thermal energy storage. Higher values of F_0 indicate that heat conduction occurs rapidly relative to the characteristics time scale of the process, and the system is close to thermal equilibrium. This number tells us how long the system takes to cool down or heat up. Therefore, as the F_0 increases, thermal diffusion becomes more effective, enabling faster distribution of heat along the transmission line during the electrical transient. A higher F_0 leads to reduce the local enhancement of losses and thus improves the overall stability of voltage and current propagation.

Figure 15 illustrates the influence of the Joule heating parameter J on the thermal distribution profile of a lossy transmission line. The figure shows that higher values of J lead to an overall rise in the thermal distribution profile. The Joule heating parameter is critical in analyzing heat generation in transmission lines, as it quantifies the conversion of electrical energy into heat energy. Increasing values of J mean more heat is generated internally in the system due to the electric current. This addition into the system raises localized heating, resulting in an increased temperature profile.

Figure 16 represents the impact of increasing the values of the dielectric heating parameter Λ on the thermal profile of a lossy transmission line. The figure indicates a rising thermal profile for higher values of Λ. This variation in the thermal profile is consistent with the physical expectations that higher values of Λ indicate greater conversion of electrical energy within dielectric materials into heat. As a result, this process adds more heat to the system, thereby raising localized heating. Consequently, we observe a higher overall temperature profile along the line. Higher temperatures can lower lines' efficiency, increase sag in overhead conductors, reduce current-carrying capacity, and accelerate material degradation.

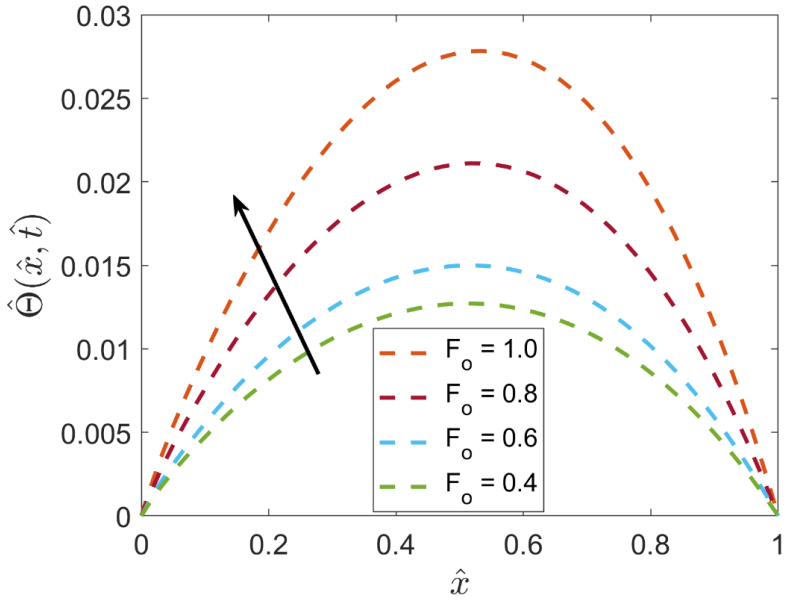

Figure 14. Variations in the thermal profile versus thermal Fourier number F_0 when$\alpha = 0.5, \beta = 0.5, J = 0.45, \Lambda = 0.6,$ and $Bi = 02$.

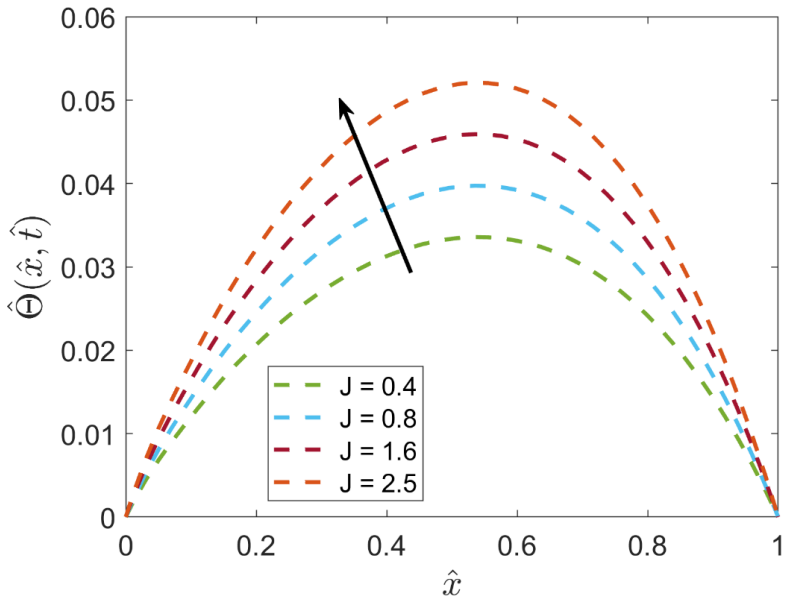

Figure 15. Variations in the thermal profile versus Joule heating parameter J when $\alpha = 0.5, \beta = 0.5, F_0 = 0.4, \Lambda = 0.6,$ and $Bi = 02$.

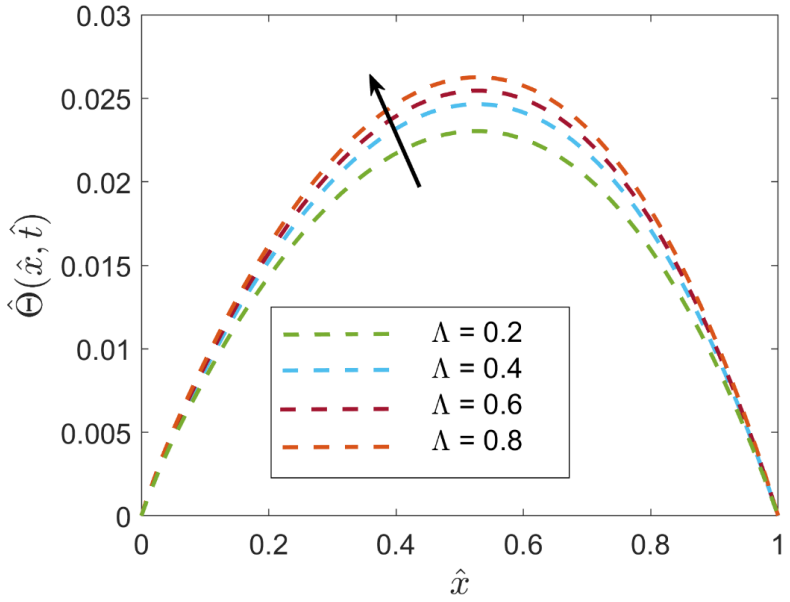

Figure 16. Variations in the thermal profile versus the dielectric heating parameter $\boldsymbol{\Lambda}$ when $\alpha = 0.5, \beta = 0.5, F_0 = 0.4, J = 0.45,$ and $Bi = 02$.

Figure 17 demonstrates how the Biot number Bi influences the thermal profile of a lossy transmission line. It is clearly seen from the figure that increasing values of Bi decrease the thermal profile. The Biot number Bi is a dimensionless parameter that characterizes the ratio of internal thermal resistance to external thermal resistance. A higher Bi indicates that more heat will be dissipated from the system, thereby causing the line to lose heat more effectively to the surrounding environment and providing improved cooling. As a result, a decreasing thermal profile is reported for higher values of Bi. This reduction in temperature also has a direct benefit by increasing the current-carrying capacity, reducing resistive heating, and reducing power attenuation along the line. Furthermore, reduced heat generation contributes to the stabilization of the dielectric properties in higher levels, which is favorable to expanding the possibilities of more efficient electric propagation. Therefore, the Biot-like number is the key factor for estimating the electro-thermal performance, efficiency, and the long-term reliability of lossy transmission lines.

The fractional and fractal orders (α, β) determine the memory degree and spatial inhomogeneity of the system, which determine how the thermal field responds to variations in the other parameters. In particular, the larger the order α is, the stronger this memory effect becomes. In other words, larger values of α make that system maintain its thermal past with a longer time scale and to take more time for reaching steady state. On the other hand, the of fractal order β introduces the degree of a spatial nonlocal behavior which modifies the diffusion pathways of thermal energy, leading to smoother or more dispersed temperature gradients.

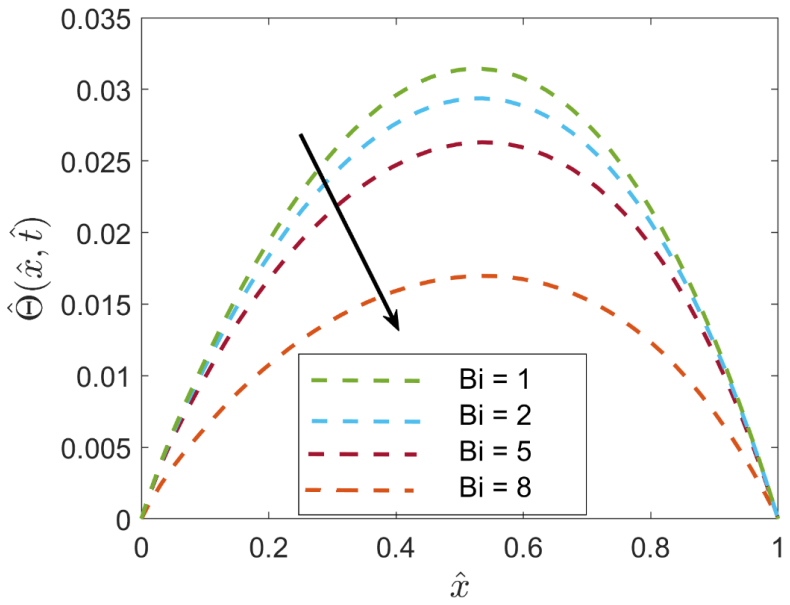

Figure 17. Variations in the thermal profile versus the Biot number Bi when $\alpha = 0.5, \beta = 0.5, F_0 = 0.4, J = 0.45, and\ \Lambda = 02$.

These effects interact considerably with the thermal contributions. The thermal source parameter J exerts a pronounced influence on the energy dissipation behavior of the system. The thermal memory effect is manifested through a reduction in cooling energy for increased values of J and lower values of either α or Bi, indicating stronger energy retention within the medium. The Biot number (Bi) also interact closely with the fractional–fractal parameters; for lower values of α and β, conductive heat transfer becomes more effective between the surface and its surrounding. Furthermore, the heat generation coefficient (F_0) and the dielectric heating parameter (Λ) are significantly modulated by the fractional and fractal operators. This modulation leads to more diffusion, producing spatially smoother and more uniform temperature distributions, whereas smaller fractional-fractal orders induce sharp temperature gradients and localized heating zones.

Figure 18 provides a comparative analysis of results obtained from the finite difference method (FDM) and LRBF scheme for the normalized thermal distribution $\hat{\imath}(\hat{x},\hat{t})$,along the $\hat{x}$-axis. Both the profiles show strong agreement for the case $\alpha = \beta = 1$. The close agreement between the two curves demonstrates that the LRBF scheme reproduces the results of the conventional FDM with high precision, confirming the accuracy, stability, and reliability of the proposed numerical approach. Figure 19 represents the absolute error of the finite difference method and the present (LRBF) method. Since the analytical solution to the problem considered is not available in literature as per our knowledge, the numerical results obtained using the finite difference method (FDM) with 500 uniformly distributed nodes are adopted as a reference solution. The results computed by the proposed LRBF method are then compared against this reference to assessing the accuracy and reliability of the developed numerical scheme. The corresponding absolute error has been computed in detail and is presented in Table 1.

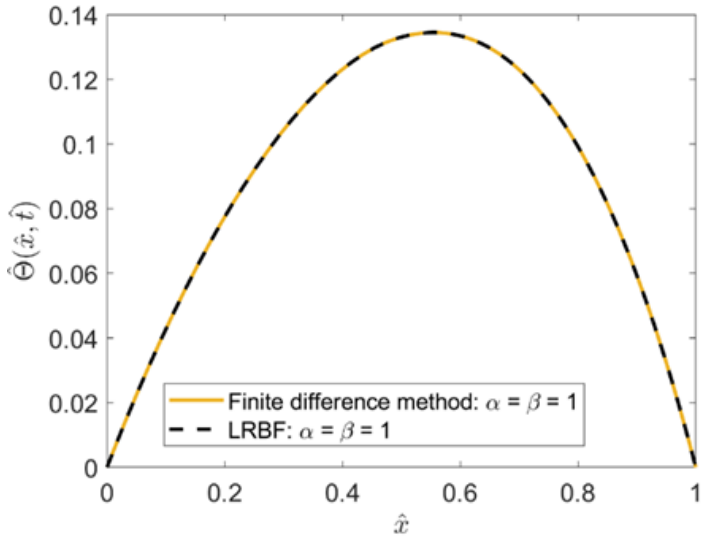

Figure 18. Solution comparison of the finite difference method and the present (LRBF) method.

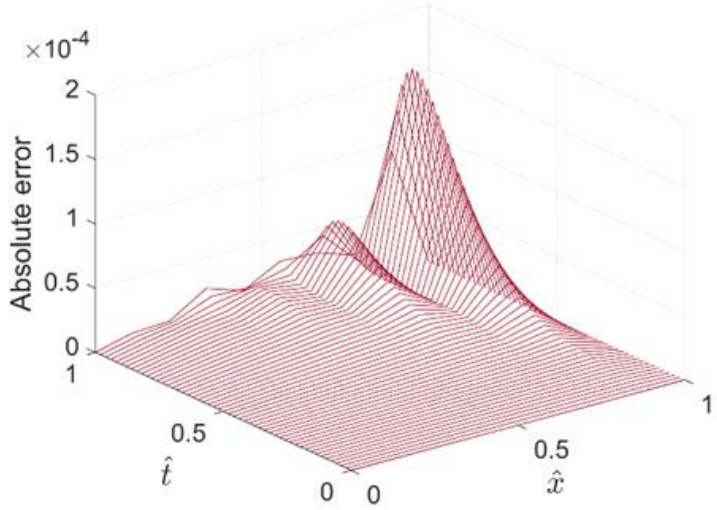

Figure 19. Absolute error of the finite difference method and the present (LRBF) method.

Table 1. Comparison of the finite difference method and the present (LRBF) method, when $\alpha = 0.5, \beta = 0.5, N = 51, F_0 = 0.4, J = 0.45, \Lambda = 0.2,$ and $Bi = 02$.

	t = 0.25			t = 0.50			t = 1		
x	FDM	LRBF	Absolute Error	FDM	LRBF	Absolute Error	FDM	LRBF	Absolute Error
0.2	0.0025109	0.0025226	1.18E-05	0.0210385	0.0210255	1.30E-05	0.0795829	0.0795595	2.34E-05
0.4	0.0054359	0.0054255	1.04E-05	0.0536038	0.0536267	2.29E-05	0.1197594	0.1197175	4.19E-05
0.6	0.0166034	0.0166216	1.82E-05	0.0808625	0.0808956	3.32E-05	0.1304321	0.1304625	3.05E-05
0.8	0.0356399	0.0356745	3.47E-05	0.0714903	0.0714214	6.89E-05	0.0976327	0.0974555	1.77E-04

5. Conclusions

In this work, an advanced and novel fractal-fractional model is formulated to analyze the propagation of voltage and current in a lossy transmission line along with thermal feedback. Numerical simulations are performed using the LRBF scheme, considering the influence of distributed parameters such as series resistance, inductance, shunt conductance, capacitance, temperature-dependent losses, the Fourier number, Joule heating, the Biot-like number, and dielectric heating along with fractal and fractional orders. This study provides a deep insight into how these parameters influence the propagation and thermal distribution along the line. The findings emphasize the importance of accounting for memory and non-local effects when assessing the performance and reliability of modern transmission systems.

- The results indicate that the fractal-fractional order parameter (α, β) has a significant impact on the thermal field of lossy transmission lines.
- In the figures, it is observed that all the integral curves converge a to steady state depending on the value of (α, β).
- In a comparative study, it has been noticed that the fractal-fractional order model exhibits more pronounced memory characteristics compared with the classical, fractional and fractal order models.
- The results indicate that voltage and current propagation exhibit a decreasing trend with increasing values of the distributed parameters series resistance $\widehat{R}$, inductance $\hat{L}$, conductance $\hat{G}$, and capacitance $\widehat{C}$.
- It is noted that the thermal field is a continuous and increasing function of the parameters $F_0, J,$ and Λ but decreasing function of Bi.

Author contributions

Saqib Murtaza, Lilia El Amraoui, and Chemeseddine Maatki conceptualized the study and developed the methodology. Data curation and software implementation were carried out by Ahmad Mir and Muhammad N. Khan. Aceng Sambas performed the formal analysis and visualization, while the investigation was jointly conducted by Saqib Murtaza and Muhammad N. Khan. Funding acquisition and resource support were provided by Aceng Sambas, Badar M. Alsharmari, and Liousa Kolsi, who also supervised and administered the project. The original draft was prepared by Saqib Murtaza, and all authors contributed to the review and editing of the manuscript. All authors have read and approved the final version of the paper.

Use of Generative-AI tools declaration

The authors declare they have not used Artificial intelligence (AI) tools in the creation of this article.

Acknowledgments

Princess Nourah bint Abdulrahman University Researchers Supporting Project number (PNURSP2025R831), Princess Nourah bint Abdulrahman University, Riyadh, Saudi Arabia. The authors extend their appreciation to the Deanship of Scientific Research at Northern Border University, Arar, KSA for funding this research work through the project number "NBU-FPEJ-2025-2928-04".

Conflict of interest

The authors declare no competing interests.

References

1. F. Rachidi, A review of field-to-transmission line coupling models with special emphasis to lightning-induced voltages on overhead lines, *IEEE T. Electromagn. C.*, **54** (2012), 898–911. https://doi.org/10.1109/TEMC.2011.2181519
2. A. J. Fairbanks, A. M. Darr, A. L. Garner, A review of nonlinear transmission line system design, *IEEE Access*, **8** (2020), 148606–148621. https://doi.org/10.1109/ACCESS.2020.3015715
3. F. D. Paolo, *Networks and devices using planar transmissions lines*, CRC Press, 2018. https://doi.org/10.1201/9781315220369
4. S. G. Talocia, H. M. Huang, A. E. Ruehli, F. Canavero, I. M. Elfadel, Transient analysis of lossy transmission lines: An efficient approach based on the method of characteristics, *IEEE T. Adv. Packaging*, **27** (2004), 45–56. https://doi.org/10.1109/TADVP.2004.825467
5. A. J. Gruodis, C. S. Chang, Coupled lossy transmission line characterization and simulation, *IBM J. Res. Dev.*, **25** (1981), 25–41. https://doi.org/10.1147/rd.251.0025
6. C. H. Kannan, V. Venugopal, P. Mathur, D. G. Kurup, Accurate modeling and performance analysis of a two-port coaxial transmission line for material characterization, In: *2024 IEEE 6th PhD Colloquium on Emerging Domain Innovation and Technology for Society (PhD EDITS)*, 2024. https://doi.org/10.1109/PhDEDITS64207.2024.10838651
7. H. Cory, S. H. Shiran, The importance of losses in the coupling of transmission lines, *IEEE T. Electromagn. C.*, **30** (1988), 567–570. https://doi.org/10.1109/15.8772
8. A. R. Djordjevic, T. K. Sarkar, R. F. Harrington, Analysis of lossy transmission lines with arbitrary nonlinear terminal networks, *IEEE T. Microw. Theory*, **34** (1986), 660–666. https://doi.org/10.1109/TMTT.1986.1133414
9. E. G. Ribas, C. D. Martinez, M. J. G. Morales, Complex analysis of the lossy-transmission line theory: A generalized smith chart, *Turk. J. Elec. Engin.*, **14** (2006), 173–194.
10. H. Mooijweer, *Derivation of the telegraphers' equations*, In: Microwave Techniques, London, 1971. https://doi.org/10.1007/978-1-349-01065-3_9
11. M. G. M. Hussain, Mathematical model for the electromagnetic conductivity of lossy materials, *J. Electromagnet. Wave.*, **19** (2005), 271–279. https://doi.org/10.1163/1569393054497311
12. O. M. Bamigbola, M. M. Ali, M. O. Oke, Mathematical modeling of electric power flow and the minimization of power losses on transmission lines, *Appl. Math. Comput.*, **241** (2014), 214–221. https://doi.org/10.1016/j.amc.2014.05.039

13. V. I. Korzyuk, J. V. Rudzko, Classical solution of the first mixed problem for the telegraph equation with a nonlinear potential, *Differ. Equ.*, **58** (2022), 175–186. https://doi.org/10.1134/S0012266122020045
14. D. P. Patil, S. Borse, D. Kapadi, Applications of Emad-Falih transform for general solution of telegraph equation, *Int. J. Adv. Res. Sci. Eng. Technol.*, **9** (2022), 19450–19454.
15. S. Hussen, M. Uddin, M. R. Karim, An efficient computational technique for the analysis of telegraph equation, *J. Eng. Adv.*, **3** (2022), 104–112. https://doi.org/10.38032/jea.2022.03.005
16. G. M. Alam, S. A. Avdonin, N. B. Avdonina, Solving forward and control problems for telegrapher's equations on metric graphs, *Math. Rep.*, **24** (2022), 3–21.
17. M. E. Köksal, Recent developments of numerical methods for analyzing telegraph equations, *Arch. Comput. Methods Eng.*, **30** (2023), 3509–3527. https://doi.org/10.1007/s11831-023-09909-w
18. K. K. Ali, M. S. Mohamed, M. Maneea, Advanced semi-analytical techniques for the q-fractional Ivancevic option pricing model, *Ain Shams Eng. J.*, **16** (2025), 103645. https://doi.org/10.1016/j.asej.2025.103645
19. U. Younas, J. Muhammad, M. A. S. Murad, D. K. Almutairi, A. Khan, T. Abdeljawad, Investigating the truncated fractional telegraph equation in engineering: Solitary wave solutions, chaotic and sensitivity analysis, *Res. Eng.*, **25** (2025), 104489. https://doi.org/10.1016/j.rineng.2025.104489
20. J. Malinzi, A mathematical model for oncolytic virus spread using the telegraph equation, Commun. *Nonlinear Sci.*, **102** (2021), 105944. https://doi.org/10.1016/j.cnsns.2021.105944
21. K. A. Abro, A. Atangana, I. Q. Memon, A. Aziz, Analytical and fractional model for power transmission of lossy transmission line, *Int. J. Model. Simul.*, **2024** (2024), 1–10. https://doi.org/10.1080/02286203.2024.2377898
22. Z. Ahmad, S. Crisci, S. Murtaza, G. Toraldo, Numerical insights of fractal-fractional modeling of magnetohydrodynamic Casson hybrid nanofluid with heat transfer enhancement, *Math. Method. Appl. Sci.*, **47** (2024), 9046–9066. https://doi.org/10.1002/mma.10059
23. A. Atangana, J. F. Gómez-Aguilar, Numerical approximation of Riemann-Liouville definition of fractional derivative: From Riemann-Liouville to Atangana-Baleanu, *Numer. Meth. Part. D. E.*, **34** (2018), 1502–1523. https://doi.org/10.1002/num.22195
24. C. Shu, H. Ding, K. S. Yeo, Local radial basis function-based differential quadrature method and its application to solve two-dimensional incompressible Navier-Stokes equations, *Comput. Method. Appl. M.*, **192** (2003), 941–954. https://doi.org/10.1016/S0045-7825(02)00618-7
25. G. E. Fasshauer, *Meshfree approximation methods with Matlab*, World Scientific, 2007.
26. H. Wendland, Local polynomial reproduction and moving least squares approximation, *IMA J. Numer. Anal*., **21** (2001), 285–300. https://doi.org/10.1093/imanum/21.1.285
27. P. D. Lax, Weak solutions of nonlinear hyperbolic equations and their numerical computation, *Commun. Pure Appl. Math.*, **7** (1954), 159–193. https://doi.org/10.1002/cpa.3160070112